ACS Photonics

Article

pubs.acs.org/journal/apchd5

Thermo-optical Effect in Phase-Change Nanophotonics

Matthias Stegmaier,[†] Carlos Ríos,[‡] Harish Bhaskaran,[‡] and Wolfram H. P. Pernice*[,†,§]

[†]Institute of Nanotechnology, Karlsruhe Institute of Technology, 76344 Eggenstein-Leopoldshafen, Germany

[‡]Department of Materials, University of Oxford, Parks Road, Oxford OX1 3PH, U.K.

[§]Department of Physics, University of Münster, 48149 Münster, Germany

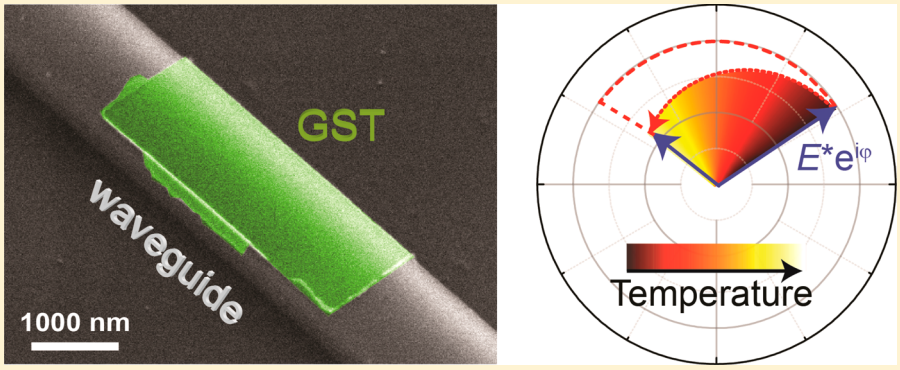

ABSTRACT: Phase-change materials (PCMs) integrated with nanophotonic components enable tunable integrated optical devices and hold promise for emerging applications in long-term photonic data storage by exploiting the large contrast in optical properties when switched between amorphous and crystalline phase states. The phase transitions rely on short heat pulses, which can be conveniently supplied by optical means. Therefore, a proper understanding of the temperature-induced refractive index fluctuations, the thermo-optical effect, is essential for controlled and optimized device operation. Here we analyze the thermo-optical effect of $Ge_2Sb_2Te_5$ nanojunctions integrated atop nanophotonic waveguides at telecommunication wavelengths. We extract the thermo-optical coefficients for the crystalline and amorphous phase state, both the real and imaginary part. We observe sign reversal of the thermo-optical coefficient upon phase change, which we trace back to different chromatic dispersion of the two phase states within the studied spectral regime. Our findings will allow for designing PCM-based modulators, nonvolatile memory systems, and reconfigurable photonic devices.

KEYWORDS: *integrated optics, all-optical, optical memory, phase-change material, nanophotonics*

The performance limitation of modern computer systems by the transfer rate between memory and processor[1] (the so-called *von-Neumann bottleneck*) has triggered intense research on optimized multicore computer architectures and on alternative communication links to conventional copper wires. Concerning the latter, optical telecommunication[2,3] is considered a promising solution to speed up the information transfer due to powerful modulation schemes such as wavelength-division multiplexing (WDM) with transfer rates exceeding Tb/s. However, in contrast to long-distance communication, where data transfer via optical fibers outmatched electronics decades ago, on shorter distances the power and time-consuming signal conversion between the electronic (processor and memory) and the optical (link) domain has prevented the use of light as the information carrier in real world applications.[4] To avoid such redundant signal conversions, a fully integrated all-optical memory[5] is required. However, to date, integrated optical memories have been predominantly volatile.[6−8] Due to their restriction to short-term data storage, such memories are not suitable for an optics-only data link.

Recently, phase-change materials (PCMs)[9,10] have emerged as suitable candidates for building an integrated all-optical nonvolatile memory.[11−13] In particular, their full compatibility with photonic circuitry and their convenient multilevel capability make them attractive candidates for future all-optical memory architectures or even non-von Neumann computing schemes.[14] PCMs, first commercialized in rewritable optical-disc storage and recently heavily investigated for the next generation of electronic random-access memory,[15] combine several beneficial properties for nonvolatile memory applications. In particular, a high refractive index contrast between their amorphous and crystalline phase enables storing information in their crystallographic phase.[16] Since these phase states (and therefore the stored information) have been demonstrated to be stable for years,[10] the respective memory can truly be viewed as nonvolatile. Furthermore, studies on the most common composition, $Ge_2Sb_2Te_5$ (GST), have shown that the phase transitions can be carried out on subnanosecond time scales;[17] low degradation can allow for up

Received: January 15, 2016
Published: April 20, 2016

ACS Publications © 2016 American Chemical Society

DOI: 10.1021/acsphotonics.6b00032
ACS Photonics 2016, 3, 828−835

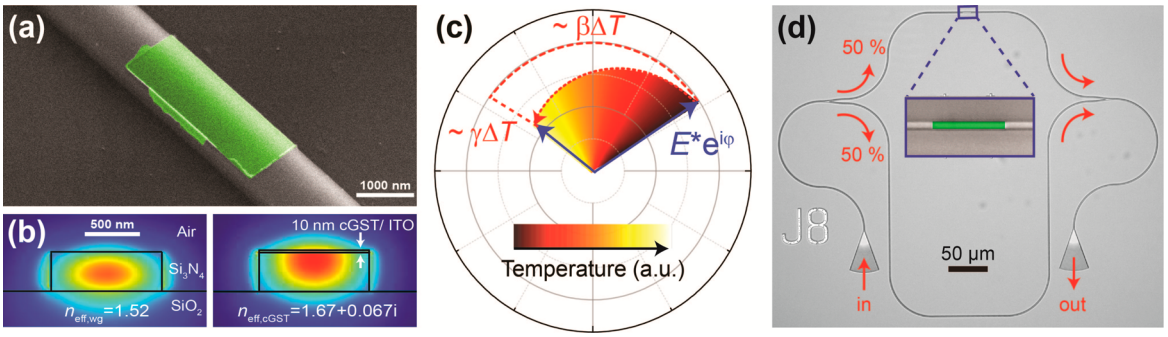

Figure 1. (a) Scanning electron micrograph of a 10 nm thick GST cell (green colored) of a 1 × 3 μm^2 footprint on top of an on-chip silicon nitride optical waveguide. (b) Finite-element simulations of the waveguide mode without (left) and with (right) crystalline GST on top. Evanescent interaction between the guided light and the GST changes the waveguide mode and thus the complex refractive index that the guided light experiences. (c) Schematic visualization of the influence of the thermo-optical effect of GST on the guided light. The electric field of the guided mode is plotted in the complex plane; that is, the radial component represents its amplitude (E) and the angular component its phase (φ). With increasing temperature (visualized with different colors) the electric field experiences both an additional phase shift (rotation by $\beta\Delta T$) and attenuation (decrease of amplitude by $\gamma\Delta T$). The effect is exaggerated and plotted not to scale for clarity. (d) Optical micrograph of an on-chip Mach–Zehnder interferometer with an embedded GST cell.

to 10^{12} switching cycles;[15] and PCM cells are scalable down to nanometric sizes.[18] Generally, PCM cells are switched between their two phases by suitable optically or electrically provided heat stimuli. For amorphization the PCM temperature is raised above the melting temperature and subsequently melt-quenched by a rapid cool down. In contrast, crystallization is triggered by heating the cell above the glass transition temperature, long enough for the atoms to form long-range order.

Since both phase transitions are temperature-driven, a proper understanding of the heating process and its influence on the switching dynamics is essential to optimize device designs and switching schemes. In particular, the temperature dependence of the real and imaginary refractive index, n and k, respectively, usually referred to as the thermo-optical effect, has to be taken into account for on-chip photonic circuitry. Generally, this relationship is in good first-order approximation linear in the temperature change ΔT and thus well described by the material-specific thermo-optical coefficients β and γ:

$$n(T_0 + \Delta T) = n_0 + \beta\Delta T \quad k(T_0 + \Delta T) = k_0 + \gamma\Delta T \tag{1}$$

For example, in silicon-on-insulator (SOI), the technically (due to well-established mass manufacturing processes) most relevant material platform, a thermo-optical coefficient of $\beta = 2 \times 10^{-4}$ 1/K[19] demands proper on-chip heat management to ensure stable operation. In contrast, material platforms such as silicon nitride,[20] aluminum nitride (AlN),[21] and diamond[22] (among others) experience a thermo-optical effect that is approximately 1 order of magnitude smaller and are thus less sensitive to temperature fluctuations. However, if these platforms are combined with PCMs, even a small thermo-optical effect of the PCM can significantly affect the device operation due to the high temperatures involved.

Here, we study the thermo-optical effect of thin-film GST layers at telecommunication wavelengths due to their emerging applications in on-chip photonic circuitry. In the first part of the paper we derive, in a two-step procedure, the thermo-optical coefficients of the on-chip hybrid GST–photonic device. We first extract the respective imaginary parts from a transmission spectrum analysis of Mach–Zehnder interferometers (MZIs) at different temperatures. Subsequently, we derive the real parts with a transient pump/probe measurement scheme, which enables selective heating of the GST cells only. Our findings demonstrate that both the real and imaginary part of the refractive index of both the amorphous and crystalline phase can change considerably during the optically induced heating process necessary for switching. For the real part we find changes of a few percent, while the imaginary part changes up to hundreds percent. We then employ finite-element simulation methods to derive the material coefficients from the measured effective ones. These thin-film parameters at telecommunication wavelengths enable the design and optimization of future nanophotonic device geometries and will allow realizing on-chip PCM-based photonic devices for all-optical nonvolatile memory, switching, modulation, and computing applications.

RESULTS AND DISCUSSION

The studied hybrid PCM–optical system comprises a GST cell on top of an on-chip Si_3N_4-based photonic waveguide, as shown in Figure 1a. Light traveling along the waveguide experiences a so-called *effective* refractive index, which is determined by not only the refractive index of the guiding material but also the exact waveguide geometry and its surrounding. Therefore, evanescent interaction of the waveguide mode with the GST results in a modification of its complex effective refractive index.[23] This is presented in Figure 1b, where the simulated mode profile (details are given in the Methods section) of both the bare waveguide (left) and the waveguide with crystalline GST on top (right) is plotted. Thus, the presence of GST alters both the phase and the amplitude of an optical wave traveling along the waveguide, which, in the case of a thermo-optical effect, also changes with increasing temperature, as sketched (exaggerated for better clarity) in Figure 1c. The change in the real part leads to a phase shift, while the change in the imaginary part leads to attenuation (dashed red lines in Figure 1c). Note, however, that the thermo-optical effect in a waveguide is not directly governed by the intrinsic material coefficients β and γ but rather by their effective counterparts β_{eff} and γ_{eff}, which, in analogy to the effective refractive index, are also influenced by the exact waveguide geometry:

$$n_{eff}(T_0 + \Delta T) = n_{eff,0} + \beta_{eff}\Delta T$$
$$k_{eff}(T_0 + \Delta T) = k_{eff,0} + \gamma_{eff}\Delta T \tag{2}$$

DOI: 10.1021/acsphotonics.6b00032
ACS Photonics 2016, 3, 828–835

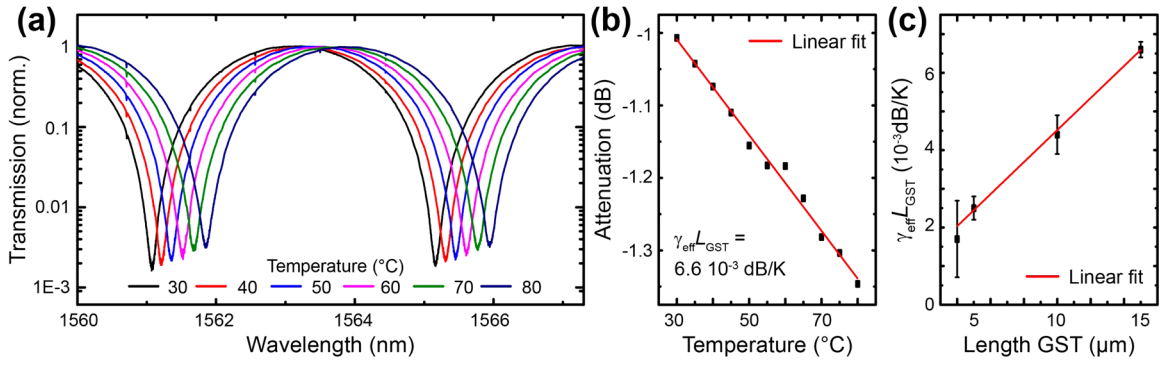

Figure 2. (a) Transmission spectrum through a MZI with an embedded aGST cell of 1 × 15 μm^2 footprint for different temperatures. Upon heating, both the real and imaginary part of the refractive index change, causing a shift of the spectrum and a decrease of the extinction ratio, respectively. (b) Change of the attenuation (absorption of the GST) within the MZI arms derived from the measured spectra and eq 4. A linear increase with increasing temperature is observed. (c) Study of the thermo-optical effect for several GST cells with different cell lengths. As expected, the effect increases linearly with cell length.

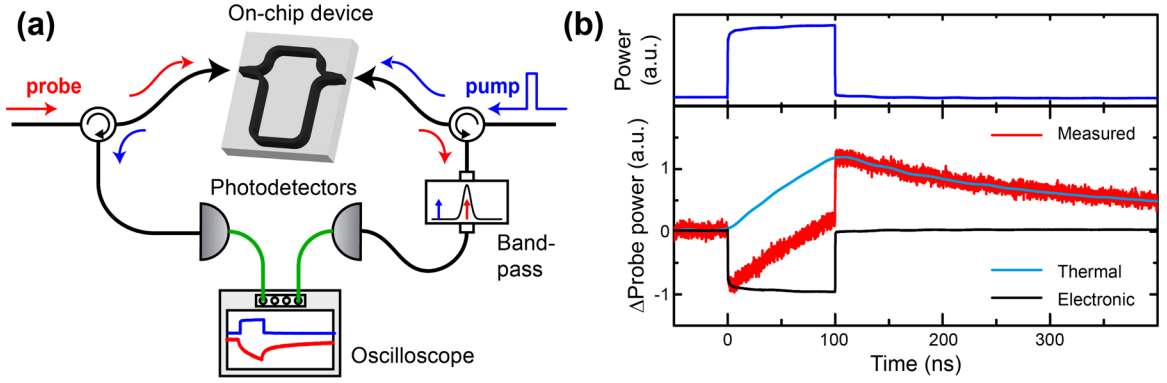

Figure 3. (a) Sketch of the used pump/probe setup. The on-chip device is characterized with an off-chip fiber-optic setup. Pump and probe lights are separated by using a bidirectional (enabled by optical circulators), two-wavelength (1545 and 1560 nm) measurement scheme. (b) Exemplary pump/probe measurement result for an aGST cell of 1 × 15 μm^2 footprint. Upon optical excitation (upper panel, blue trace), the transmitted probe power changes (lower panel, red trace) but starts to relax back to its original value directly after the end of the pump pulse. Two different contributions (thermal, light blue trace, and electronic, black trace) are identified, which can be separated since their time constants differ by 2 orders of magnitude. In contrast to the shown aGST results, in cGST cells we only observe the thermal contribution.

In the following, we derive these effective thermo-optical coefficients with on-chip MZIs. An optical micrograph of a typical device is presented in Figure 1d. As shown in the inset, the GST cell is embedded in one of the two interferometer arms. This way, a change of the refractive index of GST affects directly the amount of transmitted optical power due to interference at the combining splitter. This can be expressed as follows:[24]

$$P = \frac{1}{2}P_0\, e^{-(\alpha/2)L_{GST}}\left[\cosh\left(\frac{\alpha}{2}L_{GST}\right) + \cos(\Delta\varphi)\right]$$
$$\Delta\varphi \equiv \frac{2\pi}{\lambda}[n_{eff,wg}\Delta L - n_{eff,GST}L_{GST}] \quad (3)$$

Here, P denotes the transmitted optical power, P_0 the input power, α the waveguide power attenuation coefficient due to the GST, L_{GST} the length of the GST cell, λ the optical wavelength, ΔL the path difference between the two arms, and $n_{eff,wg}$ ($n_{eff,GST}$) the effective refractive index of the waveguide without (with) GST on top. Therefore, a change in the real part of the effective refractive index of the GST cell ($n_{eff,GST}$) results in a wavelength shift of the transmission spectrum. In contrast, the respective imaginary part ($\sim\alpha$) affects the extinction ratio.

Imaginary Part of the Thermo-optical Coefficient at Telecommunication Wavelengths. First, we study the transmission spectrum of the MZI devices at different temperatures. For that we place the chip on a proportional-integral-derivative (PID)-controlled hot plate. Exemplary data for an amorphous GST (aGST) cell of 1 × 15 μm^2 footprint are presented in Figure 2a. For clarity, the shown transmission curves are normalized separately to their maximum transmission level. Upon heating we observe both that the spectrum shifts toward higher wavelength and that the ratio of maximal (P_{max}) to minimal (P_{min}) transmitted power (extinction ratio) decreases. We note that these changes in the transmission spectrum are, since the temperature of the whole device is raised, not exclusively caused by the thermo-optical effect of GST but also by the respective ones of the SiO_2 substrate and the Si_3N_4 waveguide. Although these effects are relatively small (on the order of 10^{-5} 1/K[20]), they still dominate (by 1 order of magnitude, according to the following analysis) the observed wavelength shift because the GST cells are much smaller than the remaining circuit. In contrast, since both SiO_2 and Si_3N_4 experience negligible absorption (in our waveguides we find propagation loss as low as 0.21 dB/cm[24]) their effect on the observed increase in attenuation can be neglected. Therefore, from the measured extinction ratios we are able to extract directly the change in attenuation (thus absorption of the GST) with the following formula, which can be derived from eq 3:

DOI: 10.1021/acsphotonics.6b00032
ACS Photonics 2016, 3, 828−835

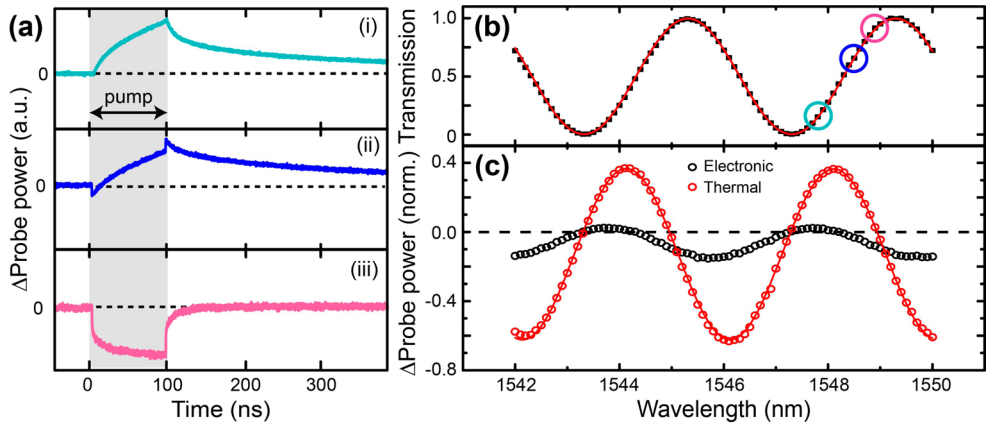

Figure 4. (a) Measured change in transmitted probe power at (i) 1547.8 nm, (ii) 1548.6 nm, and (iii) 1549 nm wavelength upon excitation with a 100 ns optical pulse at 1560 nm. The observed dependence of the change in probe power on the probe wavelength is due to the interference that takes place within the MZI. (b) Using the trace colors, the shown probe wavelengths are marked in the measured transmission spectrum of the studied MZI with an embedded 1 × 15 μm^2 aGST cell. (c) Summarized dependence on the probe wavelength for both the thermal and electronic contributions. The traces show a wavelength shift relative to the transmission spectrum and are asymmetric around zero, indicating that both the real and imaginary part of the refractive index change upon excitation. From the shown fit of eq 6 to the thermal trace, the quotient of the thermo-optical coefficients can be extracted.

$$\exp\left(-\frac{\alpha}{2}L_{GST}\right) = \left(\sqrt{\frac{P_{max}}{P_{min}}} - 1\right)\left(\sqrt{\frac{P_{max}}{P_{min}}} + 1\right)^{-1} \quad (4)$$

The corresponding results are plotted in Figure 2b for the 1 × 15 μm^2 device. In accordance with eq 2, a linear relationship is observed from which we are able to extract first the product of an effective thermo-optical coefficient γ_{eff} with the length of the GST cell, L_{GST}. To extract the value for γ_{eff}, we carry out the same analysis for several devices with different GST lengths, as presented in Figure 2c. From the expected linear relationship we can eventually obtain γ_{eff}. From this analysis and the corresponding one for cGST, we derive

$$\gamma_{eff,aGST} = (1.17 \pm 0.03) \times 10^{-5}\ K^{-1}$$
$$\gamma_{eff,cGST} = (1.13 \pm 0.03) \times 10^{-4}\ K^{-1} \quad (5)$$

Putting this in relation to the measured attenuation coefficients at room temperature (given in the Methods section) reveals that the aGST cell experiences a stronger increase of its attenuation coefficient (0.77%/K) than the cGST cell (0.17%/K).

Real Part of the Thermo-optical Coefficient. As discussed in the previous section, the thermo-optical effects of the SiO_2 substrate and the Si_3N_4 waveguide prevent the derivation of the real part of the thermo-optical coefficient of GST from the measured shifts in the device spectrum, as the one shown in Figure 2a. Therefore, we use a pump/probe measurement scheme that enables us to raise the temperature of the GST cells only.[11] This selective heating is possible since nanosecond optical pump pulses, which are sent into the device, are almost exclusively absorbed by the GST. Thermal diffusion also heats the underlying waveguide, but since both this temperature increase during the optical excitation and the thermo-optical effect of silicon nitride are comparatively small, this effect can be neglected. Off-chip, as sketched in Figure 3a, we use two optical circulators to redirect both the pump pulse and probe light first to the chip and then to the detectors. Back-reflections of the pump pulse at the interface between off-chip fibers and the on-chip device are filtered out by using two different wavelengths for the pump (1560 nm) and probe (around 1545 nm) and a color-selective bandpass filter.

In Figure 3b we present an exemplary measurement result for an aGST cell of 1 × 15 μm^2 footprint. Upon excitation with an optical 100 ns pulse (blue trace, upper panel), the transmitted optical power (lower panel, red trace) starts to relax back to its original value immediately after the end of the pump pulse. Besides the thermo-optical effect (light blue trace) we also observe an electronic contribution (black trace), which follows directly the optical pump pulse. Here, the electronic contribution is due to additional free carriers, generated by the absorbed light, which enhance the light absorption by contributing to the intraband absorption rate.[25] The thermal and electronic effects can be well separated from each other due to their inherently different time constants: while heat diffuses out of the GST within a few hundred nanoseconds, the electrons relax back within less than 300 ps (measurement is limited by the speed of the pulse generator), as shown in Figure 4a. This is consistent with pump/probe measurements carried out in the visible spectrum, where relaxation times of a few picoseconds have been observed.[26] In Figure 3b, the shown thermal trace is obtained by subtracting the electronic contribution from the measured curve and subsequent smoothing (FFT filter, 50 MHz) for clarity. In contrast, the electronic part is obtained directly from the measured pump pulse (upper panel) by rescaling it in such a way that the resulting thermal trace is continuous. In cGST we do not observe any significant electronic contribution, which means that the thermo-optical effect clearly dominates operation in this phase state.

To study the transient behavior of the GST embedded in a MZI, we perform a series of pump/probe measurements where the pump (both power and wavelength) is fixed while the probe wavelength is varied. Exemplary results are plotted in Figure 4a. It can be seen that the transient behavior depends considerably on the probe wavelength. This is a property of an MZI in which the refractive index in only one arm is varied, as discussed below. We perform the pump/probe measurements over two free spectral ranges of the MZI transmission spectrum (Figure 4b). For each wavelength a time-domain trace as in

DOI: 10.1021/acsphotonics.6b00032
ACS Photonics 2016, 3, 828−835

Figure 4a is recorded. The obtained traces are then separated into their electronic and thermal parts. The thermal contributions are obtained by analyzing the measured change in probe power 5 ns after the end of the excitation. At this time, all electronic contributions are already relaxed back, but considerable thermal diffusion has not set in yet. The shown electronic contributions are, on the other hand, taken from the measured trace 3 ns (rise time of the detector) after the start of the pump pulse, where thermal contributions are still small. In these traces the fast variation is assumed to be electronic, while the slow increase is attributed to thermal effects (see curves (ii) and (iii)). In Figure 4c we present the respective changes in probe light due to the two contributions for all measured probe wavelengths. Here, however, we want to focus on the thermo-optical effect only, and therefore the shown electronic curve is just added for clarity.

For a quantitative analysis we combine eqs 2 and 3. We assume that the thermo-optical effects ($\beta_{\mathrm{eff}}\Delta T$ and $\gamma_{\mathrm{eff}}\Delta T$) are small in comparison to the static material values at room temperature ($n_{\mathrm{eff,GST}}$ and k_{eff}) and Taylor expand the resulting equation to first order:

$$\frac{\Delta P}{P_0} = \underbrace{e^{-\frac{\alpha_0}{2}L_{\mathrm{GST}}}\frac{\pi}{\lambda}L_{\mathrm{GST}}\Delta T\beta_{\mathrm{eff}}}_{\equiv C} \times \left[\sin(\Delta\varphi_0) - \underbrace{\frac{\gamma_{\mathrm{eff}}}{\beta_{\mathrm{eff}}}}_{\equiv\delta}\cdot\left(e^{-\frac{\alpha_0}{2}L_{\mathrm{GST}}} + \cos(\Delta\varphi_0)\right)\right] \tag{6}$$

Therefore, the measured change in transmitted power ΔP depends not only on the thermo-optical coefficients but also on the phase difference $\Delta\varphi_0 = \Delta\varphi(T = T_0)$ (cf. eq 3) between the two interferometer arms and thus the probe wavelength. This equation can now be fitted to the experimental data to extract the ratio of the thermo-optical coefficients, which we term δ in the following. To do so, we first use eq 3 to extract $\exp(-\alpha_0 L_{\mathrm{GST}}/2)$ and $\Delta\varphi_0$ from the measured transmission spectrum of the device, as shown in Figure 4b. In a second step we then fit eq 6, keeping everything fixed but C and δ, to the pump/probe data. As can be seen from Figure 4c, we obtain very good agreement between the fitted curve and the experiment. We do this analysis for several devices with different GST lengths and take the ensemble average of the resulting values for δ. With the already known values of γ_{eff} as derived in the previous section we can then obtain an effective β_{eff}. From this analysis we get for the two phase states of GST

$$\begin{aligned}\beta_{\mathrm{eff,aGST}} &= (3.5 \pm 0.4) \times 10^{-5}\ \mathrm{K}^{-1}\\ \beta_{\mathrm{eff,cGST}} &= -(6.5 \pm 0.09) \times 10^{-5}\ \mathrm{K}^{-1}\end{aligned} \tag{7}$$

Setting this again in relation to the measured values at room temperature (given in the Methods section), upon heating, the effective refractive index of the aGST cell changes by 2.2×10^{-3} %/K and that of the cGST cell by -3.9×10^{-3} %/K. Furthermore, we want to emphasize that the observed change in the refractive index can, as assumed earlier, indeed be attributed only to the GST. In aGST the observed effect is more than twice as large as the pure Si_3N_4-based effect (we measure $\beta_{\mathrm{eff,Si3N4}} = 1.6 \times 10^{-5}$ 1/K). In contrast, in cGST the magnitude of the effect exceeds that of silicon nitride by a factor of 4, and, more importantly, the refractive index decreases with temperature, while in silicon nitride it increases.

We attribute this sign change upon switching to the fact that aGST experiences at 1550 nm optical wavelength (0.8 eV) normal dispersion, whereas cGST shows anomalous dispersion,[27] as shown in Figure 5. While in the amorphous phase

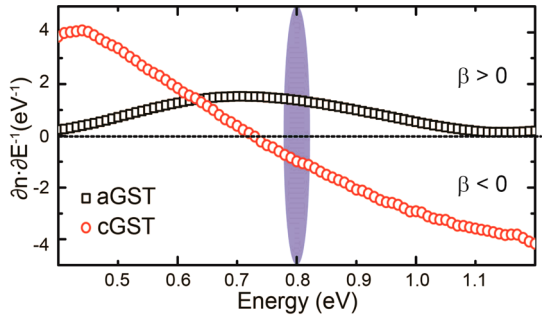

Figure 5. Derivative of the refractive index n with respect to the optical energy E, calculated from the dielectric function of GST.[27] At 1550 nm optical wavelength (0.8 eV, marked blue) aGST experiences normal dispersion but cGST, anomalous. The sign difference explains the observed sign change of β upon switching according to eq 8.

state the curve takes only positive values within the presented spectral regime, cGST experiences a sign change at an energy of approximately 0.75 eV. This is because cGST transitions at this energy from a region of normal to anomalous dispersion. In particular, at the (blue marked in the figure) energy where the measurements in this study are performed (0.8 eV) the derivative is positive in the amorphous but negative in the crystalline phase state. This sign difference in the derivative is the reason for the sign change of β upon switching.

The optical properties of GST in the near-infrared spectrum are mainly determined by electronic interband transitions; thus the thermo-optical effect can be assumed to be in first-order approximation a result of the decrease of the optical band gap (E_g) with increasing temperature (T):[28]

$$\beta = \frac{\mathrm{d}n}{\mathrm{d}T} \approx \frac{\partial n}{\partial E_g}\frac{\partial E_g}{\partial T} \propto \frac{\partial n}{\partial E_g} \tag{8}$$

Qualitatively, the dependence of the dielectric function $\varepsilon(E)$ (and thus the refractive index) on the band gap can be described with the basic Lorentz oscillator model[29] as $\varepsilon(E) = 1 + Ne^2\hbar^2\varepsilon_0^{-1}m^{-1}(E_g^2 - E^2 - \mathrm{i}\Gamma E)^{-1}$. Within this model, a decrease of E_g results mainly in a shift of the refractive index curve as a whole to lower energies. The change of the refractive index ∂n at a fixed energy E due to such a shift of the band gap, however, is qualitatively the same as if the band gap was kept constant but the energy was increased by ∂E. Therefore, the derivative of n with respect to E_g can be well approximated by the respective derivative with respect to E. This approximation is here justified because we are only interested in a qualitative explanation of the sign change of β upon switching. However, this approximation is also quantitatively correct as long as the damping term Γ is sufficiently small and E is close to E_g: $\frac{\partial\varepsilon}{\partial E} = -\left(\frac{E}{E_g} + \mathrm{i}\frac{\Gamma}{2E_g}\right)\frac{\partial\varepsilon}{\partial E_g}$. In Figure 5 we have plotted the aforementioned derivative, calculated from the measured dielectric function of GST.[27]

Extraction of Material Coefficients. In the previous paragraph we presented the measurement of the *effective* thermo-optical coefficients β_{eff} and γ_{eff} of the studied hybrid system. We now proceed to derive from these effective

DOI: 10.1021/acsphotonics.6b00032
ACS Photonics 2016, 3, 828−835

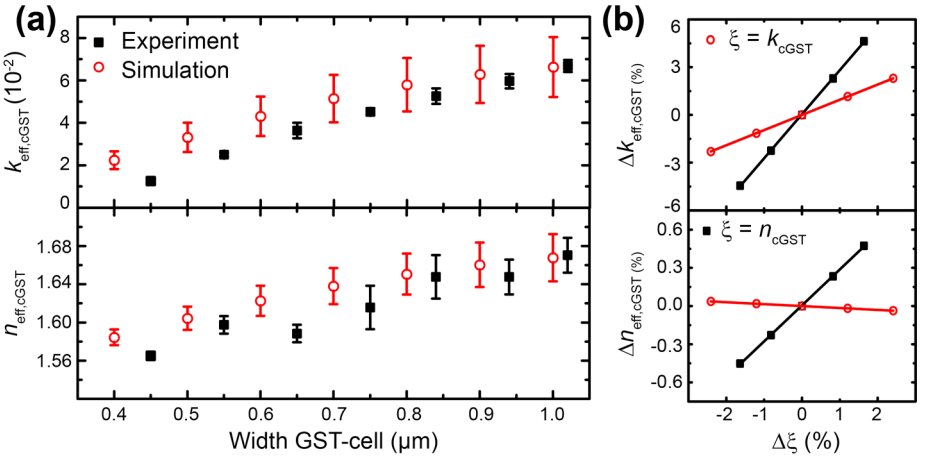

Figure 6. (a) Dependence of the imaginary (upper panel) and real (lower panel) part of the effective refractive index on the width of the cGST cell. (b) Finite-element simulation results on the dependence of the imaginary (upper panel) and real (lower panel) part of the effective refractive index on both the real and imaginary part of the refractive index of cGST. From the presented linear fits we extract the coefficients summarized in Table 1.

Table 1. Matrix Coefficients of Eq 10, Derived with COMSOL

	$\frac{\partial n_{eff,GST}}{\partial n_{GST}}$	$\frac{\partial n_{eff,GST}}{\partial k_{GST}}$	$\frac{\partial k_{eff,GST}}{\partial k_{GST}}$	$\frac{\partial k_{eff,GST}}{\partial n_{GST}}$
aGST	$(3.1 \pm 0.89) \times 10^{-2}$	$-(6.91 \pm 2.6) \times 10^{-4}$	$(3.1 \pm 0.89) \times 10^{-2}$	$(6.91 \pm 2.6) \times 10^{-4}$
cGST	$(7.7 \pm 1.4) \times 10^{-2}$	$-(3.1 \pm 0.65) \times 10^{-2}$	$(7.7 \pm 1.4) \times 10^{-2}$	$(3.1 \pm 0.65) \times 10^{-2}$

parameters the actual thin-film material coefficients using finite-element simulations (FEM). The values will, in the future, help to predict the thermo-optical effect in other device geometries used in nanophotonics.

For our analysis we study the optical waveguide mode with 2d FEM simulations on the waveguide cross-section (as shown in Figure 1b). In a first step we derive the GST cell properties at room temperature and compare the simulated effective refractive index to the measured value. When using literature values for n_{GST},[30] we observe a considerable discrepancy between our experimental findings and the simulation results. However, since our simulations without GST on top of the waveguide are in good agreement with the experiment, we attribute this difference to a refractive index of GST that deviates from the literature value. In fact, the dielectric function of GST in the infrared wavelength regime is known to depend sensitively on the exact stoichiometry of the PCM.[27] Furthermore, a considerably thinner layer (10 nm) than in the literature (100 nm) might also have an impact on the optical properties close to the band gap. Therefore, in a first step we tune the refractive index of GST by adjusting both the real and imaginary part in our simulation such that the results match our experimental findings. The unique solutions of this analysis are

$$\begin{aligned} n_{0,aGST} &= 3.94 \times (1 \pm 0.14) \\ k_{0,aGST} &= 0.045 \times (1 \pm 0.09) \\ n_{0,cGST} &= 6.11 \times (1 \pm 0.054) \\ k_{0,cGST} &= 0.83 \times (1 \pm 0.073) \end{aligned} \tag{9}$$

Using these values, the photonic structure can be modeled, in excellent agreement with experimental results, with $n_{SiO2} = 1.444$ and $n_{Si3N4} = 1.997$. Furthermore, we use $n_{ITO} = 0.6 + 0.04i$ to capture the influence of the ITO capping layer, which also has a small (in the case of cGST almost no) contribution to the evanescent coupling. This refractive index is obtained in the aforementioned process of fitting simulations to the experiment. In order to fit only one refractive index at a time, the refractive index of aGST is first derived from devices with SiO_2-capped GST cells, thus a structure without ITO, during a series of independent measurements. Then, the ITO value is adjusted such that the simulations also match the aGST/ITO structure.

To account for uncertainties in the simulation we look at the influence of all input parameter on the simulation result. Within the respective uncertainty limits, the thickness of the GST layer and the refractive index of Si_3N_4 are the most error-prone quantities. Therefore, we neglect all other sources for the error estimate and consider only a ±1 nm uncertainty (the typical thickness variation encountered in our sputtering process) of the GST-layer thickness and a refractive index variation of ±5%.

To check our simulation results, we predict from the derived values (adjusted to a 1 μm wide GST cell) the mode properties of also fabricated and measured GST cells with different widths, as shown in Figure 6a. Within the error limit our simulation results match reasonably well the experimental values. We ascribe the more rapid decrease of $k_{eff,GST}$ with decreasing cell width to a decreasing volume of the GST cell. Due to limited directionality of our used sputtering system, the cell height is slightly smaller at the edges of the cell, as qualitatively confirmed with atomic force microscopy measurements. Since the contribution of side-effects increases with decreasing cell area, this exactly leads to the observed more rapid decrease.

Next, we simulate how the effective refractive indices of the GST cell changes if the refractive index of GST is slightly varied. As shown in Figure 6b, we observe linear relationships up to changes of several percent. Therefore, the connection between the material and effective parameters can also be assumed to be linear in first-order approximation:

DOI: 10.1021/acsphotonics.6b00032
ACS Photonics 2016, 3, 828−835

$$\begin{pmatrix} \beta_{\mathrm{eff,GST}} \\ \gamma_{\mathrm{eff,GST}} \end{pmatrix} = \begin{bmatrix} \frac{\partial n_{\mathrm{eff}}}{\partial n_{\mathrm{GST}}} & \frac{\partial n_{\mathrm{eff}}}{\partial k_{\mathrm{GST}}} \\ \frac{\partial k_{\mathrm{eff}}}{\partial n_{\mathrm{GST}}} & \frac{\partial k_{\mathrm{eff}}}{\partial k_{\mathrm{GST}}} \end{bmatrix} \begin{pmatrix} \beta_{\mathrm{GST}} \\ \gamma_{\mathrm{GST}} \end{pmatrix} \tag{10}$$

Here, the matrix coefficients are just the slopes of the linear dependences observed in Figure 6b. The respective values, obtained from linear fits to the simulation data, are summarized in Table 1. The stated uncertainties are derived by repeating the same analysis as before but at the boundaries of the confidence interval in eq 9 and by taking the maximal deviation. Using these coefficients, we obtain the thermo-optical coefficients of GST by inverting eq 10:

$$\begin{aligned} \beta_{\mathrm{aGST}} &= (1.1 \pm 0.34) \times 10^{-3}\ \mathrm{K}^{-1} \\ \gamma_{\mathrm{aGST}} &= (4.1 \pm 1.2) \times 10^{-4}\ \mathrm{K}^{-1} \\ \beta_{\mathrm{cGST}} &= -(2.2 \pm 2.0) \times 10^{-4}\ \mathrm{K}^{-1} \\ \gamma_{\mathrm{cGST}} &= (1.56 \pm 0.21) \times 10^{-3}\ \mathrm{K}^{-1} \end{aligned} \tag{11}$$

In our analysis we have neglected the contribution of the ITO capping layer. This is, however, justified because it has only a little influence on the effective refractive index of the cell, as reflected by the fact that the respective coefficients are, in comparison to the ones in Table 1, over 1 order of magnitude smaller.

METHODS

The devices are fabricated from a 335 nm Si_3N_4/3350 nm SiO_2 wafer in a three-step electron-beam lithographic procedure combined with sputter deposition of GST and subsequent lift-off. The sputter-deposited GST of 10 nm thickness is capped with a 10 nm ITO layer to prevent oxidation. For further details on the fabrication we refer the reader to refs 11, 12, and 24. All waveguides are designed to be 335 nm high and 1 μm wide. The widths of the waveguides are measured after fabrication with high-resolution SEM images to be 1.02 μm. The width and the length of the GST cells are varied between 350 nm and 1 μm and between 500 nm and 15 μm, respectively. After fabrication we characterize the attenuation of both as-deposited amorphous GST (aGST) and crystalline GST (cGST). The GST is crystallized by thermal annealing on a hot plate at 200 °C for 5 min. We measure an optical attenuation coefficient (at room temperature) of 0.053 and 2.35 dB/μm and effective refractive indices of 1.57 and 1.67 for aGST and cGST cells of 1 μm width, respectively.

To characterize the on-chip devices, we couple light between the off-chip fiber setup (for more details refer to refs 11 and 31) and the on-chip devices with so-called focusing grating couplers optimized for wavelengths around 1550 nm. The transmission spectra are recorded with a tunable continuous wave (CW) laser source (Santec, TSL-510C) in combination with a low-noise photodetector (New Focus, model 2011). Optical pulses are generated from the second CW laser (New Focus, 6427) by an electro-optical modulator (Lucent Technologies, 2623CS) and an electrical pulse generator (HP 8131A) and are further amplified with an erbium-doped fiber amplifier (Pritel, LNHPFA-33). Back-reflections of the pump pulse at the interface between off-chip fibers and the on-chip device are filtered out by using two different wavelengths for pump (1560 nm) and probe (around 1545 nm) and a color-selective bandpass filter (Pritel, TFA-1550). The detector (New Focus, models 1811s and 1554-B) signals are recorded with a 6 GHz oscilloscope (Agilent Infiniium, 54855A), while averaging over 200 measurements is carried out for noise reduction.

The finite-element simulations presented in Figure 1b are carried out with COMSOL Multiphysics. The silicon nitride waveguide is modeled as a 335 nm high and 1.02 μm wide rectangle with a refractive index of 1.997 on top of a silicon dioxide substrate with $n_{\mathrm{SiO2}} = 1.444$. In accordance with our results, the 10 nm high cGST is modeled with the refractive indices given in eq 9 and the 10 nm ITO capping layer with $n_{\mathrm{ITO}} = 0.6 + 0.04i$. All simulations are carried out at a wavelength of 1550 nm.

CONCLUSION

We have experimentally shown that GST exhibits a significant thermo-optical effect at telecommunication wavelengths, which can considerably influence device operation. Using a combination of static transmission and dynamic pump/probe measurements we have derived the effective thermo-optical coefficients of the hybrid GST−photonic device. We observe that in both crystal phases the real and imaginary parts of the effective refractive index change on the order of 10^{-3} %/K and 10^{-1} %/K, respectively. Therefore, during switching, where the temperature is optically raised by several hundred Kelvins, these coefficients change by a few (real parts) up to hundreds (imaginary parts) percent, which is large enough to considerably influence operation dynamics in on-chip devices, in particular in photonic cavities. We further observe that upon switching the sign of the thermo-optical effect changes from positive (aGST) to negative (cGST), which we have attributed to a change in the dispersive properties of GST from a normal (aGST) to an anomalous (cGST) dispersion regime at the studied wavelengths around 1550 nm. Using FEM simulations we have derived the material coefficients from the measured effective ones. Our results will in the future help to optimize both the design and operation schemes of all-optical memories, switches, and modulators.

AUTHOR INFORMATION

Corresponding Author

*E-mail: wolfram.pernice@uni-muenster.de.

Notes

The authors declare no competing financial interest.

ACKNOWLEDGMENTS

The authors acknowledge support by Deutsche Forschungsgemeinschaft (DFG) grants PE 1832/1-1 and PE 1832/2-1 and EPSRC grant EP/J018783/1. C.R. is grateful to JEOL UK and the Clarendon Fund for funding his graduate studies. M.S. acknowledges support from the Karlsruhe School of Optics and Photonics (KSOP) and the Stiftung der Deutschen Wirtschaft (sdw). H.B. acknowledges support from the John Fell Fund and the EPSRC (EP/J00541X/2 and EP/J018694/1). The authors also acknowledge support from the DFG and the State of Baden-Württemberg through the DFG-Center for Functional Nanostructures (CFN) within subproject A6.4. The authors thank S. Diewald for assistance with device fabrication, M. Blaicher for technical assistance with device design, and A. Vetter, S. Ferrari, and P. Rath for helpful discussions.

DOI: 10.1021/acsphotonics.6b00032
ACS Photonics 2016, 3, 828−835

REFERENCES

(1) Kirchain, R.; Kimerling, L. A Roadmap for Nanophotonics. *Nat. Photonics* **2007**, *1* (6), 303−305.
(2) Paniccia, M. Integrating Silicon Photonics. *Nat. Photonics* **2010**, *4* (8), 498−499.
(3) Caulfield, H. J.; Dolev, S. Why Future Supercomputing Requires Optics. *Nat. Photonics* **2010**, *4* (5), 261−263.
(4) Alduino, A.; Paniccia, M. Interconnects: Wiring Electronics with Light. *Nat. Photonics* **2007**, *1* (3), 153−155.
(5) Kuramochi, E.; Notomi, M. Optical Memory: Phase-Change Memory. *Nat. Photonics* **2015**, *9* (11), 712−714.
(6) Liu, L.; Kumar, R.; Huybrechts, K.; Spuesens, T.; Roelkens, G.; Geluk, E.-J.; de Vries, T.; Regreny, P.; Van Thourhout, D.; Baets, R.; Morthier, G. An Ultra-Small, Low-Power, All-Optical Flip-Flop Memory on a Silicon Chip. *Nat. Photonics* **2010**, *4* (3), 182−187.
(7) Nozaki, K.; Shinya, A.; Matsuo, S.; Suzaki, Y.; Segawa, T.; Sato, T.; Kawaguchi, Y.; Takahashi, R. Based on Nanocavities. *Nat. Photonics* **2012**, *6* (4), 248−252.
(8) Kuramochi, E.; Nozaki, K.; Shinya, A.; Takeda, K.; Sato, T.; Matsuo, S.; Taniyama, H.; Sumikura, H.; Notomi, M. Large-Scale Integration of Wavelength-Addressable All-Optical Memories on a Photonic Crystal Chip. *Nat. Photonics* **2014**, *8* (6), 474−481.
(9) Wuttig, M.; Yamada, N. Phase-Change Materials for Rewriteable Data Storage. *Nat. Mater.* **2007**, *6* (11), 824−832.
(10) Raoux, S.; Wuttig, M. Phase Change Materials. *Annu. Rev. Mater. Res.* **2009**, *39* (1), 25−48.
(11) Ríos, C.; Stegmaier, M.; Hosseini, P.; Wang, D.; Scherer, T.; Wright, C. D.; Bhaskaran, H.; Pernice, W. H. P. Integrated All-Photonic Non-Volatile Multi-Level Memory. *Nat. Photonics* **2015**, *9* (11), 725−732.
(12) Ríos, C.; Hosseini, P.; Wright, C. D.; Bhaskaran, H.; Pernice, W. H. P. On-Chip Photonic Memory Elements Employing Phase-Change Materials. *Adv. Mater.* **2014**, *26* (9), 1372−1377.
(13) Rudé, M.; Pello, J.; Simpson, R. E.; Osmond, J.; Roelkens, G.; van der Tol, J. J. G. M.; Pruneri, V. Optical Switching at 1.55 Mm in Silicon Racetrack Resonators Using Phase Change Materials. *Appl. Phys. Lett.* **2013**, *103* (14), 141119.
(14) Wright, C. D.; Hosseini, P.; Diosdado, J. A. V. Beyond von-Neumann Computing with Nanoscale Phase-Change Memory Devices. *Adv. Funct. Mater.* **2013**, *23* (18), 2248−2254.
(15) Burr, G. W.; Breitwisch, M. J.; Franceschini, M.; Garetto, D.; Gopalakrishnan, K.; Jackson, B.; Kurdi, B.; Lam, C.; Lastras, L. A.; Padilla, A.; Rajendran, B.; Raoux, S.; Shenoy, R. S. Phase Change Memory Technology. *J. Vac. Sci. Technol. B* **2010**, *28* (2), 223−262.
(16) Wang, Q.; Rogers, E. T. F.; Gholipour, B.; Wang, C.-M.; Yuan, G.; Teng, J.; Zheludev, N. I. Optically Reconfigurable Metasurfaces and Photonic Devices Based on Phase Change Materials. *Nat. Photonics* **2016**, *10* (1), 60−65.
(17) Loke, D.; Lee, T. H.; Wang, W. J.; Shi, L. P.; Zhao, R.; Yeo, Y. C.; Chong, T. C.; Elliott, S. R. Breaking the Speed Limits of Phase-Change Memory. *Science* **2012**, *336* (6088), 1566−1569.
(18) Raoux, S.; Rettner, C. T.; Jordan-Sweet, J. L.; Kellock, A. J.; Topuria, T.; Rice, P. M.; Miller, D. C. Direct Observation of Amorphous to Crystalline Phase Transitions in Nanoparticle Arrays of Phase Change Materials. *J. Appl. Phys.* **2007**, *102* (9), 1−8.
(19) Komma, J.; Schwarz, C.; Hofmann, G.; Heinert, D.; Nawrodt, R. Thermo-Optic Coefficient of Silicon at 1550 Nm and Cryogenic Temperatures. *Appl. Phys. Lett.* **2012**, *101* (4), 041905.
(20) Arbabi, A.; Goddard, L. L. Measurements of the Refractive Indices and Thermo-Optic Coefficients of Si3N4 and SiO(x) Using Microring Resonances. *Opt. Lett.* **2013**, *38* (19), 3878−3881.
(21) Xiong, C.; Pernice, W. H. P.; Sun, X.; Schuck, C.; Fong, K. Y.; Tang, H. X. Aluminum Nitride as a New Material for Chip-Scale Optomechanics and Nonlinear Optics. *New J. Phys.* **2012**, *14* (9), 095014.
(22) Rath, P.; Ummethala, S.; Nebel, C.; Pernice, W. H. P. Diamond as a Material for Monolithically Integrated Optical and Optomechanical Devices. *Phys. Status Solidi A* **2015**, *2399* (11), 2385−2399.
(23) Pernice, W. H. P.; Bhaskaran, H. Photonic Non-Volatile Memories Using Phase Change Materials. *Appl. Phys. Lett.* **2012**, *101* (17), 171101.
(24) Gruhler, N.; Benz, C.; Jang, H.; Ahn, J.-H.; Danneau, R.; Pernice, W. H. P. High-Quality Si3N4 Circuits as a Platform for Graphene-Based Nanophotonic Devices. *Opt. Express* **2013**, *21* (25), 31678−31689.
(25) Soref, R. A.; Bennett, B. R. Electrooptical Effects in Silicon. *IEEE J. Quantum Electron.* **1987**, *23* (1), 123−129.
(26) Waldecker, L.; Miller, T. a.; Rudé, M.; Bertoni, R.; Osmond, J.; Pruneri, V.; Simpson, R. E.; Ernstorfer, R.; Wall, S. Time-Domain Separation of Optical Properties from Structural Transitions in Resonantly Bonded Materials. *Nat. Mater.* **2015**, *14* (6), 1−6.
(27) Shportko, K.; Kremers, S.; Woda, M.; Lencer, D.; Robertson, J.; Wuttig, M. Resonant Bonding in Crystalline Phase-Change Materials. *Nat. Mater.* **2008**, *7* (8), 653−658.
(28) Luckas, J.; Kremers, S.; Krebs, D.; Salinga, M.; Wuttig, M.; Longeaud, C. The Influence of a Temperature Dependent Bandgap on the Energy Scale of Modulated Photocurrent Experiments. *J. Appl. Phys.* **2011**, *110* (1), 01371910.1063/1.3605517
(29) Klingshirn, C. *Semiconductor Optics*; Graduate Texts in Physics; Springer: Berlin, Heidelberg, 2007.
(30) Kim, S. Y.; Kim, S. J.; Seo, H.; Kim, M. R. Variation of the Complex Refractive Indices with Sb-Addition in Ge-Sb-Te Alloy and Their Wavelength Dependence. *Proc. SPIE* **1998**, *3401*, 112−118.
(31) Taillaert, D.; Van Laere, F.; Ayre, M.; Bogaerts, W.; Van Thourhout, D.; Bienstman, P.; Baets, R. Grating Couplers for Coupling between Optical Fibers and Nanophotonic Waveguides. *Japanese J. Appl. Physics, Part 1 Regul. Pap. Short Notes Rev. Pap.* **2006**, *45* (8A), 6071−6077.

DOI: 10.1021/acsphotonics.6b00032
ACS Photonics 2016, 3, 828−835